JOURNAL OF COMPUTATIONAL PHYSICS 5, 139–168 (1970)

A Numerical Model for Viscous, Free-Surface, Barotropic Wind Driven Ocean Circulations

W. P. CROWLEY

Lawrence Radiation Laboratory, University of California, Livermore, California

Received May 12, 1969

As a first step in investigating the consequences of making the fixed-surface assumption in ocean circulation models, a numerical model for free-surface barotropic flow in a basin on a beta-plane is proposed. Two numerical solutions are presented. The first solution was obtained using a standard linear eddy viscosity ($\kappa = 10^8$ cm^2/sec) and it agrees with Gates' solution. The second solution was obtained using a nonlinear eddy viscosity due to Leith and based on two-dimensional turbulence arguments. The two solutions differ in that the nonlinear eddy viscosity permits an intensification of interior flows and a transient modification of the western boundary current.

I. INTRODUCTION

In modelling ocean circulations it is frequently assumed that external gravity waves influence the circulations only slightly; their exclusion from a model is thus thought to contribute only a small error to solutions obtained with the model. This assumption will be examined in this and in a second report wherein we will obtain and compare barotropic solutions from the primitive equations (the free-surface case) with barotropic solutions from the filtered equations (the fixed-surface case). The equations of motion are nonlinear, and the solutions will be obtained by numerical methods, but the conclusions reached will be pertinent to analytic studies as well. In the second report we will deal with a numerical model for the fixed-surface case and with a comparison of expected solutions (from linear theory) with realized solutions. In this report the numerical method used to obtain solutions for the free-surface case will be described. In addition, two numerical solutions obtained from two variants of the free-surface model will be presented here. The models differ in that the first one includes a linear eddy viscosity ($\kappa = 10^8$ cm^2/sec^{-1}) while the second uses instead, a nonlinear eddy viscosity.

In seeking solutions to the partial differential equations governing large scale hydrodynamic phenomena such as the circulations of the oceans, one can take three points of view with regard to the temporal aspects of the problem. One can eliminate

time from the equations by fiat and seek steady solutions. Alternately, one can find steady solutions by keeping time as an independent variable and averaging the solution over say the longest period germane to the problem [1]. The third choice is to seek time dependent solutions explicitly [2]. In analytic approaches to ocean circulation problems, the first choice is usually made except in the simplest of cases [3]. However, if one seeks numerical solutions, it is sometimes easier to solve the time dependent equations rather than the steady equations and so the second choice is often made. In obtaining these steady numerical solutions one is usually forced to integrate the equations of motion for relatively long periods of time and the problem of choosing a numerically stable but reasonably efficient time step becomes an important consideration. Efficiency is of course a desirable trait in short term problems also, but it is a much more serious consideration for the long term integrations.

For difference equations based on hyperbolic differential equations, the Courant–Freidrichs–Lewy stability condition [4] requires essentially that the time step be chosen so that any combination of signals can traverse at most one zone per time step. The largest possible time step may thus be obtained by (1) determining which phenomena are relevant to the problem at hand, and (2) removing from the solution any other phenomenon if it acts to decrease the time step. Filtering out these unwanted features is usually accomplished by modifying the equations of motion in some way [5] but this must be done carefully; even though the filtered equations may permit a larger time step to be used, they may also take longer to compute and may even result in a less efficient calculation.

For ocean circulation calculations we start with the primitive equations and note that there are several characteristic speeds that may occur in solutions. We have sound waves (5400 km/h), external gravity waves (800 km/h), internal gravity waves (4 km/h), Rossby waves (25 km/h), and currents (3 km/h). We will be concerned here with simple barotropic models, and will eliminate sound waves by assuming the flow to be incompressible, and internal gravity waves by working with vertically-integrated equations of motion. The elimination of sound waves and internal gravity waves results in a free-surface barotropic model. If external gravity waves are eliminated from the free-surface model by imposing a condition of zero vertical velocity at the top and bottom of the fluid, we have a fixed-surface model. In addition to advective and diffusive processes, fixed-surface barotropic models permit only Rossby waves to exist while free-surface barotropic models include external (surface) gravity waves as well. We expect then that the free-surface solution will be more accurate than the fixed-surface solution in that it will more closely approximate nature. It may be, however, that the barotropic solution depends primarily on Rossby waves and is only weakly influenced by the presence of gravity waves. If this is so, the fixed-surface model will generate a reasonable approximation to the barotropic solution, and we will profit by having a less

complex set of equations to solve and by being able to increase the integration time step by more than an order of magnitude.

The purpose of this series of reports then is to investigate the consequences of using the fixed-surface approximation in place of the free-surface approximation to obtain barotropic solutions.

In Sections II and III, the equations of motion and boundary conditions for free-surface flow are stated. The finite difference equations are contained in Section IV, and a stability analysis follows in Section V. A comparative discussion of two numerical solutions is presented in Section VI and a summary of this investigation is given in Section VII. Comments on the need for, and the formulation of the nonlinear eddy viscosity used here are contained in an appendix.

II. Equations of Motion

For viscous flow on a rotating sphere, the equations for the horizontal components of velocity are [6]

$$\frac{\partial u}{\partial t} + \mathbf{V} \cdot \nabla u + w \frac{\partial u}{\partial z} = -\frac{1}{\rho} \frac{\partial p}{\partial x} + fv + F^x \tag{II-1}$$

$$\frac{\partial v}{\partial t} + \mathbf{V} \cdot \nabla v + w \frac{\partial v}{\partial z} = -\frac{1}{\rho} \frac{\partial p}{\partial y} - fu + F^y \tag{II-2}$$

where $f = 2\Omega \sin \theta$ is the Coriolis parameter; (F^x, F^y) is the dissipation term; $\mathbf{V}$ is the horizontal velocity vector having an eastward component u and a northward component v; p is the pressure, ρ is the density, and w is the vertical component of velocity. In anticipation of the β-plane approximation the metric

$$dx = a \cos \theta \, d\lambda$$

$$dy = a \, d\theta$$

where a, θ, and λ are the earth's radius, the latitude, and longitude, respectively, has been introduced. For the sake of simplicity, we will eventually eliminate the convergence of coordinate lines by choosing a constant value for $\cos \theta$ in this metric.

If in addition we assert that the fluid is incompressible

$$\nabla \cdot \mathbf{V} + \frac{\partial w}{\partial z} = 0 \tag{II-3}$$

and homogeneous, in hydrostatic equilibrium

$$p(z) = p_0 + \rho g(z - h), \tag{II-4}$$

we have a system of four equations in the four unknowns u, v, w, and p. A left-handed coordinate system in which z increases "downward" is employed (Fig. 1).

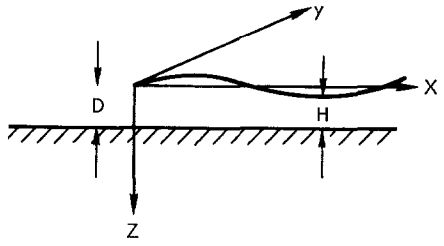

FIG. 1. Coordinate system in which x increases eastward and y increases northward.

The equilibrium depth D and the total local depth $H = D - h$ are much less than the minimum wavelength of horizontal motions permitted by the finite difference mesh (see Section III) and we thus have shallow waves with a characteristic gravity wave speed of $\sqrt{gD}$. The variations of surface height h about the equilibrium depth are such that negative values of h correspond to wave crests.

To simplify matters somewhat, and to make the solutions more amenable to analysis, the β-plane approximation is made—i.e., we assume $f = f_0 + \beta y$ when f_0 and β are constants.

We are interested primarily in the exterior flows here, and choose to eliminate the vertical structure by the use of integrals. Following Gates [2], we let an overbar indicate the following integral,

$$\bar{u}(t, x, y) = \frac{1}{H} \int_h^D u(t, x, y, z)\, dz \tag{II-5}$$

where u stands for any of the dependent variables. Differentiation of (II-5) gives, for $D = D(x, y)$ and $h = h(t, x, y)$, for example

$$\overline{\frac{\partial u}{\partial x}} = \frac{\partial \bar{u}}{\partial x} - \frac{u_D - \bar{u}}{H} \frac{\partial D}{\partial x} + \frac{u_h - \bar{u}}{H} \frac{\partial h}{\partial x} \tag{II-6}$$

If we then apply the integral from Eq. (II-5) to Eqs. (II-1), (II-2), and (II-3) we have, after some manipulation

$$\frac{\partial M}{\partial t} + \frac{\partial Mu}{\partial x} + \frac{\partial Mv}{\partial y} = gH \frac{\partial h}{\partial x} + fN + \nabla \cdot \kappa \nabla M + \tau_D^x - \tau_h^x, \tag{II-7}$$

$$\frac{\partial N}{\partial t} + \frac{\partial Nu}{\partial x} + \frac{\partial Nv}{\partial y} = gH \frac{\partial h}{\partial y} - fM + \nabla \cdot \kappa \nabla N + \tau_D^y - \tau_h^y, \tag{II-8}$$

and

$$\frac{\partial h}{\partial t} - \frac{\partial M}{\partial x} - \frac{\partial N}{\partial y} = 0, \tag{II-9}$$

where we have now dropped the overbars, let $M = Hu$, $N = Hv$, and have made closure assumptions; for the nonlinear terms,

$$\overline{Hu^2} = H\bar{u}\bar{u} \qquad \text{and} \qquad \overline{Huv} = H\bar{u}\bar{v}$$

and for the dissipative terms

$$\overline{\kappa H\nabla^2 u} = \nabla \cdot \kappa\nabla M \qquad \text{and} \qquad \overline{\kappa H\nabla^2 v} = \nabla \cdot \kappa\nabla N,$$

where κ is the horizontal eddy diffusion coefficient. In addition we have assumed that the horizontal components of bottom and surface stresses are given by

$$\tau_D^x = \kappa_v \frac{\partial u}{\partial z}\Big)_D, \qquad \tau_h^x = \kappa_v \frac{\partial u}{\partial z}\Big)_h$$
$$\tau_D^y = \kappa_v \frac{\partial v}{\partial z}\Big)_D, \qquad \tau_h^y = \kappa_v \frac{\partial v}{\partial z}\Big)_h,$$

where κ_v is the vertical eddy diffusion coefficient.

For the problems of concern here, we will take the bottom drag as well as the north-south surface stress to be zero,

$$\tau_h^y = \tau_D^y = \tau_D^x = 0 \tag{II-10}$$

and the east-west surface stress to be a simple function of y alone (Section III).

III. The Basin, Boundary Condition, and Wind Stress

The model is set up for rectangular basins L units wide and Y units high, but to contrast with Bryan [1], Fischer [7], and Gates [2] the special case considered here is that of a square basin, $L = Y = 4440$ km. The basin is subdivided into 26 zones in each direction so that mesh points are separated by approximately 170 km; the smallest wavelength permitted is thus 340 km.

Boundary conditions are somewhat a matter of personal choice—those taken here, for velocity, correspond to no-normal transport, free-slip conditions at the northern and southern boundaries and the no-slip condition at eastern and western boundaries. This then permits a viscous boundary layer to exist only along the "coastal" edges, and we have

$$M(t, 0, y) = M(t, L, y) = N(t, 0, y) = N(t, L, y) = 0$$
$$\frac{\partial M}{\partial y}\Big)_{y=0} = \frac{\partial M}{\partial y}\Big)_{y=Y} = N(t, x, 0) = N(t, x, Y) = 0.$$

The application of these boundary conditions to Eq. (II-8) results in a subsidiary condition along the eastern and western boundaries,

$$gH \frac{\partial h}{\partial y}\Big)_{x=0,L} + \frac{\partial}{\partial x} \kappa \frac{\partial N}{\partial x}\Big)_{x=0,L} = 0. \tag{III-1}$$

To conserve volume, the surface height anomaly h is permitted to change in time along the boundaries, but discussion of this will be deferred to Section IV.

As noted in Section II all components of the surface stress and bottom drag are zero except for the east-west surface-stress term, and it is taken to be

$$\tau_h^x = K_D \cos \pi y / Y, \tag{III-2}$$

where K_D is 0.004 km^2 h^{-2}. The curl of the wind stress is thus zero only at the northern and southern boundaries, and a separation of the "gulf stream" [8] is not anticipated.

The Coriolis parameter is linearized in accordance with the β-plane approximation

$$f = f_0 + \beta y, \tag{III-3}$$

where $f_0 = 0.18$ h^{-1} and $\beta = 0.63 \times 10^{-4}$ km^{-1} h^{-1}. The basin thus starts at a latitude of 20° and extends to 60°. The choice of β corresponds to a latitude of 40°.

IV. Difference Equations

In this section, we shall set down the difference approximations to Eqs. (II-7), (II-8), and (II-9) and the boundary conditions on h deferred from Section III.

The dependent variables are taken to be staggered in both space and time; forward time differences and stabilized, centered space differences are used. If n, k, and l are indices associated with the indepedent variables t, x, and y, we have $h(t_n, x_k, y_l) = h(n\,\Delta t, k\,\Delta x, l\,\Delta y) = h^n_{k,l}$ and $M^{n-1/2}_{k-1/2,l-1/2}$ and $N^{n-1/2}_{k-1/2,l-1/2}$. The south-west corner of the mesh is shown in Fig. 2A to illustrate the spatial relation of the dependent variables. A section of the (x, t) projection of the space-time mesh is shown in Fig. 2B.

The conservative nature of the differential equations is carried over into the formulation of the difference equations. That is, rather than thinking of $h_{k,l}$ as a point-wise quantity, it is considered to be a mean value over some local spatial region, namely the rectangle between the vertical lines $x_{k-1/2}$ and $x_{k+1/2}$ and the horizontal lines $y_{l-1/2}$ and $y_{l+1/2}$. In Fig. 2A then h is associated with the zone enclosed by broken lines while M and N are associated with zones enclosed by solid lines.

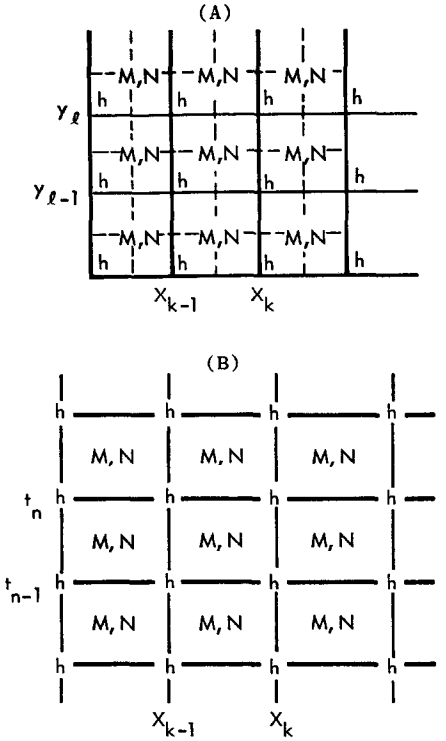

FIG. 2. (A) Southwest corner of the mesh showing the spatial relation of the variables M, N, and h. (B) A projection of the (x, y, t) space onto the (x, t) plane showing the space-time relation of the variables M, N, and h.

To illustrate the conservative aspects of the equations of motion more fully, Eqs. (II-7) and (II-8) are rewritten

$$\frac{\partial M}{\partial t} = -\frac{\partial FM}{\partial x} - \frac{\partial GM}{\partial y} + gH\frac{\partial h}{\partial x} + fN - \tau_h^x \tag{IV-1}$$

and

$$\frac{\partial N}{\partial t} = -\frac{\partial FN}{\partial x} - \frac{\partial GN}{\partial y} + gH\frac{\partial h}{\partial y} - fM, \tag{IV-2}$$

where the operators F and G are

$$F = u - \kappa\frac{\partial}{\partial x}$$

and

$$G = v - \kappa\frac{\partial}{\partial y}.$$

The fluxes FM, GM, FN, and GN thus account for the advection and diffusion of momentum, and if these quantities can be computed along the solid lines (Fig. 2A) we are well on the way to determining the tendencies of M and N.

We take the momentum fluxes to be

$$\frac{2\Delta t}{\Delta x}(FM)_{k,l-1/2} = \alpha_{k,l-1/2}(M_{k+1/2,l-1/2} + M_{k-1/2,l-1/2}) - (\alpha^2_{k,l-1/2} + 2\beta)(M_{k+1/2,l-1/2} - M_{k-1/2,l-1/2}) \quad \text{(IV-3)}$$

and

$$\frac{2\Delta t}{\Delta y}(GM)_{k-1/2,l} = \alpha_{k-1/2,l}(M_{k-1/2,l+1/2} + M_{k-1/2,l-1/2}) - (\gamma^2_{k-1/2,l} + 2\delta)(M_{k-1/2,l+1/2} - M_{k-1/2,l-1/2}), \quad \text{(IV-4)}$$

where $\alpha = u\,\Delta t/\Delta x$, $\beta = \kappa\,\Delta t/\Delta x^2$, $\gamma = v\,\Delta t/\Delta y$, and $\delta = \kappa\,\Delta t/\Delta y^2$.

The advective part of these fluxes (the remainder with $\kappa = 0$) is derived and analyzed elsewhere [9]. It is sufficient to note here that in the one-dimensional case, the condition for stability is

$$(u\,\Delta t/\Delta x)^2 + 2(\kappa\,\Delta t/\Delta x^2) < 1$$

when forward time differences are used, and when only advection and diffusion are accounted for.

The algorithm for advancing quantities in time is based on the Marchuk [10] time-splitting method, and we have

$$M^* = M^{n-1/2} - \frac{\Delta t}{\Delta x}[FM^{n-1/2})_{k,l-1/2} - FM^{n-1/2})_{k-1,l-1/2} - Kh)^n_{k-1/2,l-1/2}], \quad \text{(IV-5a)}$$

$$N^* = N^{n-1/2} - \frac{\Delta t}{\Delta x}[FN^{n-1/2})_{k,l-1/2} - FN^{n-1/2})_{k-1,l-1/2}], \quad \text{(IV-5b)}$$

$$M^{**} = M^* - \frac{\Delta t}{\Delta y}[GM^*)_{k-1/2,l} - GM^*)_{k-1/2,l-1}] + \Delta t\tau^x_h)_{k-1/2,l-1/2}, \quad \text{(IV-6a)}$$

$$N^{**} = N^* - \frac{\Delta t}{\Delta y}[GN^*)_{k-1/2,l} - GN^*)_{k-1/2,l-1} - Lh)^n_{k-1/2,l-1/2}], \quad \text{(IV-6b)}$$

$$M^{n+1/2} = M^{**} + f\,\Delta t\,N^{n+1/2}, \quad \text{(IV-7a)}$$

and

$$N^{n+1/2} = N^{**} - f\,\Delta t\,M^{n+1/2}, \quad \text{(IV-7b)}$$

where a subscript $(k - 1/2,\ l - 1/2)$ is understood for all M and N, and the operators K and L are given by

$$Kh)_{k-1/2,l-1/2} = \frac{g}{8}[4D - h_{k,l} - h_{k,l-1} - h_{k-1,l} - h_{k-1,l-1}] \times [h_{k,l} + h_{k,l-1} - h_{k-1,l} - h_{k-1,l-1}]$$

and

$$Lh)_{k-1/2,l-1/2} = \frac{g}{8}[4D - h_{k,l} - h_{k,l-1} - h_{k-1,l} - h_{k-1,l-1}] \times [h_{k,l} + h_{k-1,l} - h_{k,l-1} - h_{k-1,l-1}].$$

Equations (IV-5) are solved for M^* and N^* at all mesh points. Then Eqs. (IV-6) are solved for M^{**} and N^{**} at all mesh points. Finally $M^{n+1/2}$ and $N^{n+1/2}$ are computed at all mesh points from equations resulting from Eqs. (IV-7).

It is emphasized that the fluxes computed from Eqs. (IV-3) and (IV-4) are based on intermediate (perhaps starred) values of M and N, but on values of u and v only at time $(n - 1/2)\,\Delta t$.

The surface height anomaly is then advanced in time,

$$h_{k,l}^{n+1} = h_{k,l}^{n} + \frac{\Delta t}{2\Delta x}[M_{k+1/2,l+1/2}^{n+1/2} + M_{k+1/2,l-1/2}^{n+1/2} - M_{k-1/2,l+1/2}^{n+1/2} - M_{k-1/2,l-1/2}^{n+1/2}] + \frac{\Delta t}{2\Delta y}[N_{k+1/2,l+1/2}^{n+1/2} + N_{k-1/2,l+1/2}^{n+1/2} - N_{k+1/2,l-1/2}^{n+1/2} - N_{k-1/2,l-1/2}^{n+1/2}] \qquad \text{(IV-8)}$$

by solving Eq. (IV-8) at all *interior* mesh points. At boundary points, special precautions must be taken to insure that volume and momentum are conserved, and these are dealt with in the remainder of this section.

All boundary calculations involve use of the method of images whereby image points outside the mesh are introduced and functional values are determined at these points through the boundary conditions and the equations of motion. This technique considerably simplifies some of the programming aspects of the problem.

At the northern boundary, we have a slip, no-transport boundary condition;

$$N_{k-1/2,\mathscr{L}} = 0$$

and

$$\frac{\partial M}{\partial y}\Big)_{k-1/2,\mathscr{L}} = 0$$

for $1 \leqslant k \leqslant K$. These conditions are satisfied to second order if images at $\mathscr{L} + 1/2$ are given by

$$N_{k-1/2,\mathscr{L}+1/2} = -N_{k-1/2,\mathscr{L}-1/2}$$

and

$$M_{k-1/2,\mathscr{L}+1/2} = M_{k-1/2,\mathscr{L}-1/2}.$$

Along the eastern boundary we have a no-slip boundary condition

$$M_{K,l-1/2} = N_{K,l-1/2} = 0$$

for $1 \leqslant l \leqslant \mathscr{L}$ and it would appear that the conditions

$$M_{K+1/2,l-1/2} = -M_{K-1/2,l-1/2}$$

and

$$N_{K+1/2,l-1/2} = -N_{K-1/2,l-1/2}$$

would give satisfactory images in this case as in the slip-boundary case. Pragmatically this is not true, apparently because the viscous boundary layer associated with the no-slip boundary condition is not adequately represented.

An improved estimate for the images is obtained from Eq. (III-1)

$$\kappa \frac{\partial^2 N}{\partial x^2}\Big)_{K,l-1/2} + gH \frac{\partial h}{\partial y}\Big)_{K,l-1/2} = 0$$

so that now the tangential component of momentum, N, at the image point will involve the viscosity coefficient.

The no-slip (eastern) boundary conditions are thus

$$M_{K+1/2,l-1/2} = -M_{K-1/2,l-1/2}$$

and

$$N_{K+1/2,l-1/2} = N_{K-1/2,l-1/2} - \frac{g\Delta x^2 D}{4\kappa \Delta y}(h_{K,l} - h_{K,l-1})$$

for $1 \leqslant l \leqslant \mathscr{L}$.

The functional values so constructed at image points permit the diffusive flux to be evaluated at all boundaries and it is seen that the diffusion of tangential momentum along slip boundaries is zero. The normal advective flux along all boundaries is set to zero, in accordance with the no-transport boundary condition.

Boundary conditions on the surface height anomaly h reflect the no (normal) transport conditions and are imposed so that volume is conserved. Along the northern boundary,

$$h^{n+1}_{k,\mathscr{L}} = h^n_{k,\mathscr{L}} + (M^{n+1/2}_{k+1/2,\mathscr{L}-1/2} - M^{n+1/2}_{k-1/2,\mathscr{L}-1/2})\frac{\Delta t}{\Delta x} - (N^{n+1/2}_{k+1/2,\mathscr{L}-1/2} + N^{n+1/2}_{k-1/2,\mathscr{L}-1/2})\frac{\Delta t}{\Delta y}$$

and along the eastern boundary

$$h^{n+1}_{K,l} = h^n_{K,l} - (M^{n+1/2}_{K-1/2,l+1/2} + M^{n+1/2}_{K-1/2,l-1/2})\frac{\Delta t}{\Delta x} + (N^{n+1/2}_{K-1/2,l+1/2} - N^{n+1/2}_{K-1/2,l-1/2})\frac{\Delta t}{\Delta y}.$$

That is, the tangential flux of h along the northern (slip) boundary is M while the tangential flux along the eastern (no-slip) boundary is N. Thus, for example, in the north-east corner we have

$$h^{n+1}_{K,\mathscr{L}} = h^{n}_{K,\mathscr{L}} \quad 2M^{n+1/2}_{K-1/2,\mathscr{L}-1/2}\frac{\Delta t}{\Delta x} - 2N^{n+1/2}_{K-1/2,\mathscr{L}-1/2}\frac{\Delta t}{\Delta y}.$$

These relations are easily derived if the terms $\partial M/\partial x + \partial N/\partial y$ in Eq. (II-9) are recognized as the divergence of a flux. The differential equation is then integrated over the appropriate area (dotted box in Fig. 2A) and Green's theorem permits the transformation of the divergence expression into line integrals over the surface of the dotted box. Division by the area of the zone completes the derivation.

Along southern and western boundaries the boundary conditions are similar to those just described for northern and eastern boundaries, respectively.

A calculation cycle proceeds as follows assuming we have h^n, $M^{n-1/2}$, $N^{n-1/2}$ for all spatial points. Equations (IV-5), (IV-6), and (IV-7) are solved giving $M^{n+1/2}$ and $N^{n+1/2}$. During this part of the computation the image points are set up as needed using h^n and the intermediate (starred) values of M and N. Finally h^{n+1} is computed by Eq. (IV-8) (with appropriate modifications in boundary points) at all spatial points.

V. Stability Analysis

In this section, a stability analysis of the difference equations from Section IV is undertaken. The equations are linearized and arranged so that matrix notation may be employed. For nonboundary points, the (complex) third-order characteristic polynomial for the eigenvalues of the amplification matrix is derived and the eigenvalues are determined numerically.

We define the finite difference operators

$$\begin{aligned}(Au)_{k,l} &= u_{k+1,l} - u_{k-1,l},\\ (Bu)_{k,l} &= u_{k+1,l} - 2u_{k,l} + u_{k-1,l},\\ (Cu)_{k,l} &= u_{k,l+1} - u_{k,l-1},\\ (Du)_{k,l} &= u_{k,l+1} - 2u_{k,l} + u_{k,l-1}.\end{aligned}$$

In terms of A, B, C, and D we define

$$R_1 = I - \frac{\alpha}{2}A + \left(\frac{\alpha^2}{2} + \beta\right)B$$

and

$$R_2 = I - \frac{\gamma}{2}C + \left(\frac{\gamma^2}{2} + \delta\right)B,$$

where I is the identity operator, $\alpha = u\,\Delta t/\Delta x$, $\gamma = v\,\Delta t/\Delta y$, $\beta = \kappa\,\Delta t/\Delta x^2$, $\delta = \kappa\,\Delta t/\Delta y^2$.

We define P, Q, S, and T by

$$(Ph)_{k-1/2,l-1/2} = \frac{g\Delta t}{2\Delta x}(h_{k,l} + h_{k,l-1} - h_{k-1,l} - h_{k-1,l-1}),$$

$$(Qh)_{k-1/2,l-1/2} = \frac{g\Delta t}{2\Delta y}(h_{k,l} + h_{k-1,l} - h_{k,l-1} - h_{k-1,l-1}),$$

$$(Su)_{k,l} = \frac{H\Delta t}{2\Delta x}(u_{k+1,l+1} + u_{k+1,l} - u_{k,l+1} - u_{k,l}),$$

and

$$(Tu)_{k,l} = \frac{H\Delta t}{2\Delta y}(u_{k+1,l+1} + u_{k,l+1} - u_{k+1,l} - u_{k,l}).$$

In terms of these operators and the constant $F = f\,\Delta t$, a calculation cycle for the linearized equations is given by the matrix equation

$$V^{n+1} = \Lambda_4\Lambda_3\Lambda_2\Lambda_1 V^n = \Lambda V^n,$$

where

$$V^n = \begin{pmatrix} u^{n-1/2}_{k-1/2,l-1/2} \\ v^{n-1/2}_{k-1/2,l-1/2} \\ h^n_{k,l} \end{pmatrix}$$

and

$$\Lambda_1 = \begin{pmatrix} R_1 & 0 & P \\ 0 & R_1 & 0 \\ 0 & 0 & I \end{pmatrix},$$

$$\Lambda_2 = \begin{pmatrix} R_3 & 0 & 0 \\ 0 & R_3 & Q \\ 0 & 0 & I \end{pmatrix},$$

$$\Lambda_3 = \begin{pmatrix} \dfrac{I}{1+F^2} & \dfrac{F}{1+F^2} & 0 \\ \dfrac{-F}{1+F^2} & \dfrac{I}{1+F^2} & 0 \\ 0 & 0 & I \end{pmatrix},$$

$$\Lambda_4 = \begin{pmatrix} I & 0 & 0 \\ 0 & I & 0 \\ S & T & I \end{pmatrix}.$$

If we assume that the spatial behavior of these functions can be represented by complex exponentials and use linearity to suppress summations, we have

$$u_{k,l} = \bar{u}_{pq}(t)\, \epsilon^{i(kp\Delta x + lq\Delta y)},$$

$$v_{k,l} = \bar{v}_{pq}(t)\, \epsilon^{i(kp\Delta x + lq\Delta y)},$$

and

$$h_{k,l} = \bar{h}_{pq}(t)\, \epsilon^{i(kp\Delta x + lq\Delta y)}$$

and the operators then become

$$A = 2i \sin p\Delta x,$$

$$B = 2(\cos p\Delta x - 1)$$

$$C = 2i \sin q\Delta y,$$

$$D = 2(\cos q\Delta y - 1),$$

$$P = \frac{g\Delta t}{2\Delta x}(1 + \epsilon^{-iq\Delta y})(1 - \epsilon^{-ip\Delta x}),$$

$$Q = \frac{g\Delta t}{2\Delta y}(1 + \epsilon^{-ip\Delta x})(1 - \epsilon^{-iq\Delta y}),$$

$$S = -\frac{H\Delta t}{2\Delta x}(1 + \epsilon^{iq\Delta y})(1 - \epsilon^{ip\Delta x}),$$

and

$$T = -\frac{H\Delta t}{2\Delta y}(1 + \epsilon^{ip\Delta x})(1 - \epsilon^{iq\Delta y}).$$

In general, the eigenvalues ξ of the amplification matrix Λ are complex. Since the flows under consideration here are physically stable, a necessary condition for numerical stability is $\xi\xi^* \leqslant 1$.

To simplify somewhat the determination of ξ, we assume $p\,\Delta x = q\,\Delta y = \phi$, $\alpha = \gamma$, $\beta = \delta$, and $\Delta x = \Delta y$. It follows then that $R_1 = R_3 = R$, $P = Q$, and $S = T$ and the characteristic equation reduces to

$$(1 + F^2)\xi^3 - (W + 2R^2)\xi^2 + \{R^4 + R^2[2 + QT(1 + R)]\}\xi - R^4 = 0, \quad \text{(V-1)}$$

where

$$W = TQ[1 + F + R(1 - F)] + 1 + F^2.$$

Since this is a cubic with complex, rather complicated coefficients, a closed form solution will presumably not be of much help. We choose rather to compute the roots of the characteristic equation based on fixed values of the parameters κ, u, Δx, gH, and f. We increase Δt in discrete steps from a small value (for which

$\xi\xi^* \leqslant 1$) until the magnitude of one of the eigenvalues just exceeds unity for $0 \leqslant \phi \leqslant \pi$. This value of Δt minus the increment is then taken as the maximum allowable time increment for the given set of parameters. Values of Δt determined in this manner are given in Figs. 3 for $gH = 5.08 \times 10^4$ km^2 h^{-2}. In Figs. 3A and 3B, $\Delta x = 170$ km while in Figs. 3C and 3D $\Delta x = 85$ km the latter being necessary since the momentum points are separated from the boundary by only 85 km. Each figure is plotted for a specific value of κ and each curve is parameterized by a

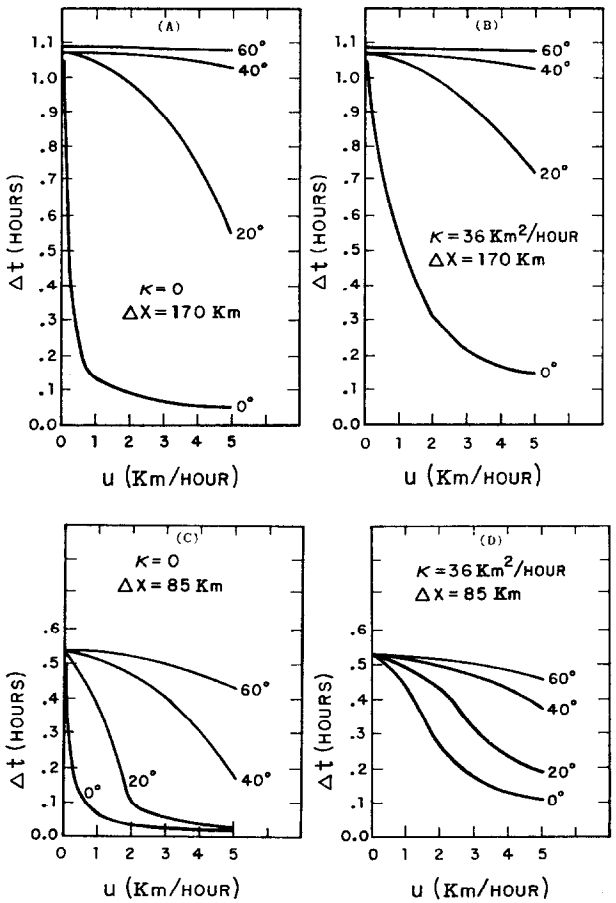

FIG. 3. (A) and (B) Plots of maximum allowable time step (Δt) versus advective velocity as determined numerically through a linear stability analysis. Each curve is parameterized by the latitude via the Coriolis parameter f. The left curve is for zero viscosity and $\Delta x = 170$ km; the right curve is for $\kappa = 36$ km^2/h and $\Delta x = 170$ km. (C) and (D) Similar to curves in (A) and (B) except that here $\Delta x = 85$ km rather than 170 km.

specific value of f. It is seen that an increase in both f and κ leads to a relaxation of the maximum allowable Δt. For f this is understandable since the implicit formulation of the Coriolis acceleration introduces some amplitude damping [6]. For κ this behavior is not easily understood from simple ideas. It turns out though that when $\beta \sim 0.1$ in Eq. (V-1), this effect is felt, and a further increase in κ does necessitate a decrease in Δt.

It is found experimentally that the model is unstable for $\Delta t = 0.25$ h but is stable for $\Delta t = 0.125$ h. In Fig. 3D this Δt is found for $u \sim 5$ km/h at the (minimum) latitude of 20°. It appears then that the gross simplifications that have gone into this analysis have permitted us to estimate a stable integration time step to within a factor of three.

VI. Results

In this section, some calculational results will be presented and superficially discussed. A thorough analysis of the transient phase of the free-surface solution has already been given by Gates [2]—the results obtained with this model substantiate his findings in general. However, the model presented here differs from Gates' model in at least three ways. A rather insignificant difference is that the basin used here is square in opposition to the rectangular shape preferred by Gates. In addition, the wind stress coefficient is larger here. The most significant difference though is that the results presented here were obtained with a nonlinear eddy viscosity. It will be seen that this permits small scale features to develop; at the same time, it prevents them from contributing to aliassing errors (see Appendix I).

From the given constant zonal wind-stress we expect from conservation of angular momentum that a large-scale clockwise rotation of the fluid will occur. Since the Coriolis parameter is an increasing function of latitude, we also expect a westward intensification of the flow [11]—i.e., we anticipate the formation of a "gulf stream" near the western boundary. Superposed on this fundamental mode we can expect to find two types of damped waves; vertical-transverse gravity waves due to the free-surface and horizontal-tranverse Rossby waves due to the variation of the Coriolis parameter with latitude [5]. The gravity waves have a phase velocity, $\sqrt{gH}$, of 220 km/h and the Rossby waves have a phase velocity of ~25 km/h. (The trapped Rossby waves featured in this solution have a phase velocity of ~4 km/h and a group velocity of ~3 km/h.) Moreover, the Rossby wave phase velocity never has an eastward component—to satisfy energy conservation requirements at a rigid wall, however, the group velocity may have an eastward component [12].

The transient aspects of the solution may be inferred from Figs. 4A and 4B; these are plots of the kinetic and potential energies for the nonlinear and the linear viscosity cases, respectively. For the nonlinear case, there is a spin-up time of

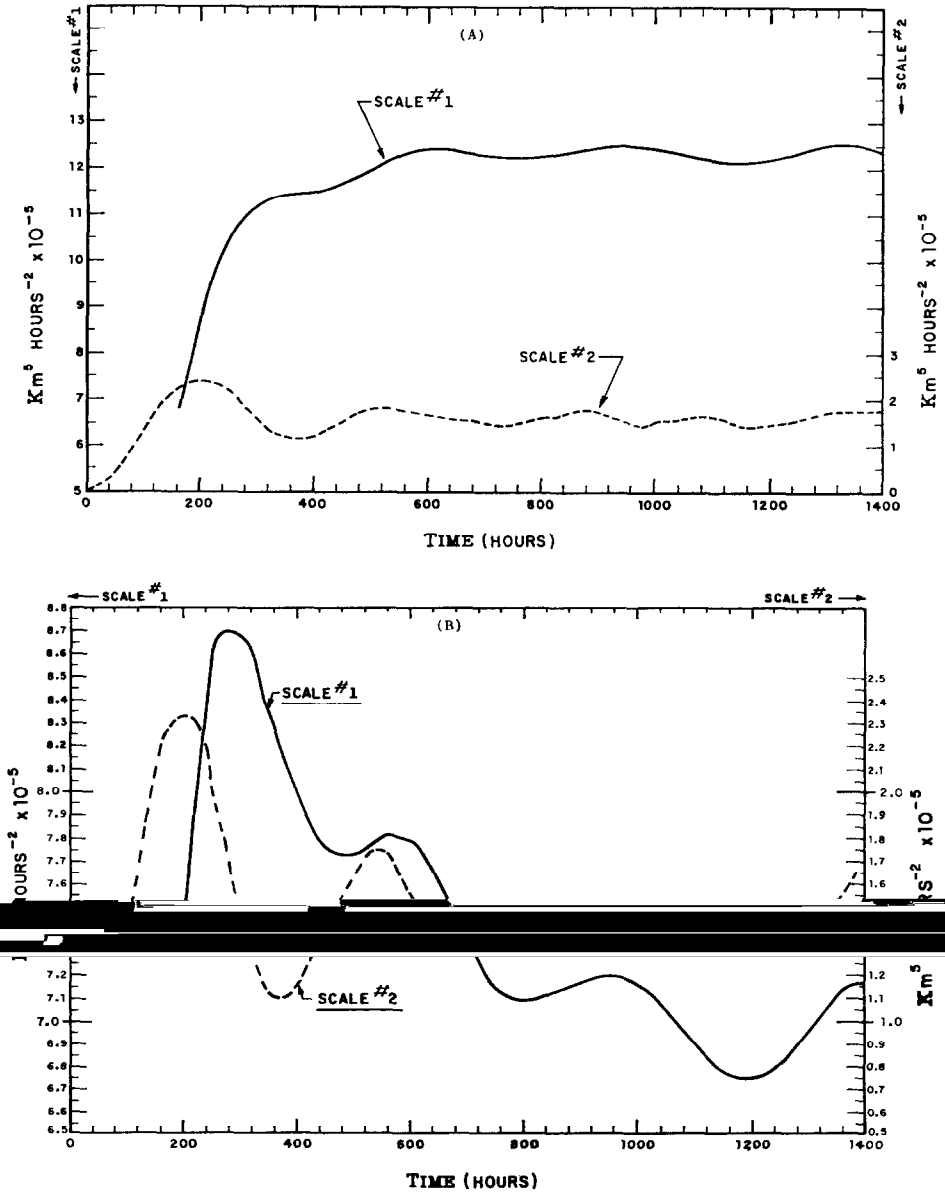

FIG. 4. (A) Total kinetic and potential energies energies as a function of time for the nonlinear viscosity case. The solid curve gives $\frac{1}{2}\iint (Mu + Nv)\,dx\,dy$ (these values range between 5 and 13×10^5 km^5 h^{-2}). The broken curves gives $\frac{1}{2}\iint gh^2\,dx\,dy$ and these values range between 0 and 3×10^5 km^5 h^{-2}. (B) Total kinetic and potential energies as a function of time for the case of a linear viscosity. The solid curve gives $\frac{1}{2}\iint (Mu + Nv)\,dx\,dy$ (these values range between 6.5 and 8.8×10^5 km^5 h^{-2}). The broken curve gives $\frac{1}{2}\iint gh^2\,dx\,dy$ and these values range between 0.5 and 2.5×10^5 km^5 h^{-2}.

600 h, approximately twice that of the linear case. After the spin-up time, the kinetic energy in the two cases oscillates with a period of ~340 h, but it is an initially damped oscillation in the linear case. (Times of 300 and 600 h may be identified with the Rossby wave reflected from the western boundary—this reflection creates alternate cells of southward and northward currents, and the first two northward cells east of the "gulf stream" appear at times of approximately 300 and 600 h as will be seen in Figs 8 and 11.) The natural period for the (1,1) mode in this basin is 346 h.

Details of the transient solution (with nonlinear viscosity) are seen by comparing contour maps of the dependent variables h, M, and N at different times (see Figs. 5 through 19). These contour maps are computer produced (subject to linear interpolation between mesh points) plots of calculated data. The data have been subjected neither to additional smoothing (other than that in the basic finite difference equations) not to artistic enhancement. Solid lines represent positive or zero values of the function being plotted and broken lines represent negative values. The contour intervals for h and M are 30 cm and 0.025 $km^2\ h^{-1}$, respectively. The occurrence of the "gulf stream" means that to resolve data in the eastern part of the basin, plots of N must be separated into two parts, N and N_2. Plots of N cover the entire basin and have a contour interval of 0.08 $km^2\ h^{-1}$. Plots of N_2 omit the first two western mesh points and have a contour interval of 0.015 $km^2\ h^{-1}$. The propagation of Rossby waves is seen most readily in plots of N, and only a few plots of h and M are presented.

The initial condition for this example is taken to be a state of rest with $h = M = N = 0$.

Figures 5 through 12 are contour plots of N_2 at four day intervals extending from day 1 through day 29. The structure and wavelength of the evolving Rossby wave pattern is evident in these plots. The northeastern tilt of these cells is a nonlinear effect emphasized by the choice of a large wind stress coefficient. If K_D is reduced by a factor of 3, to correspond with the nominal physical value [8], the tilt disappears and the cells are almost vertical. This is probably related to Veronis' solution; he was able to move the gulf-stream from the western boundary to the northern boundary by substantially increasing the Rossby number [13].

Figure 13 is a plot of the complete north-south velocity field N at day 29. It exhibits the gross structure of the Rossby wave pattern as well as the western boundary current implied by the plot of N_2.

Figures 14 through 19 show the east-west velocity field and the surface height distribution at days 5, 17, and 29. It is seen from these figures that the flow is for the most part geostrophically balanced.

Figures 20, 21, and 22 are contour plots of N, M, and h at day 29 for the case of linear viscosity. A comparison of Figs. 13 and 20 (N at day 29) shows that the same pattern appears in both solutions but that the nonlinear solution is more intense.

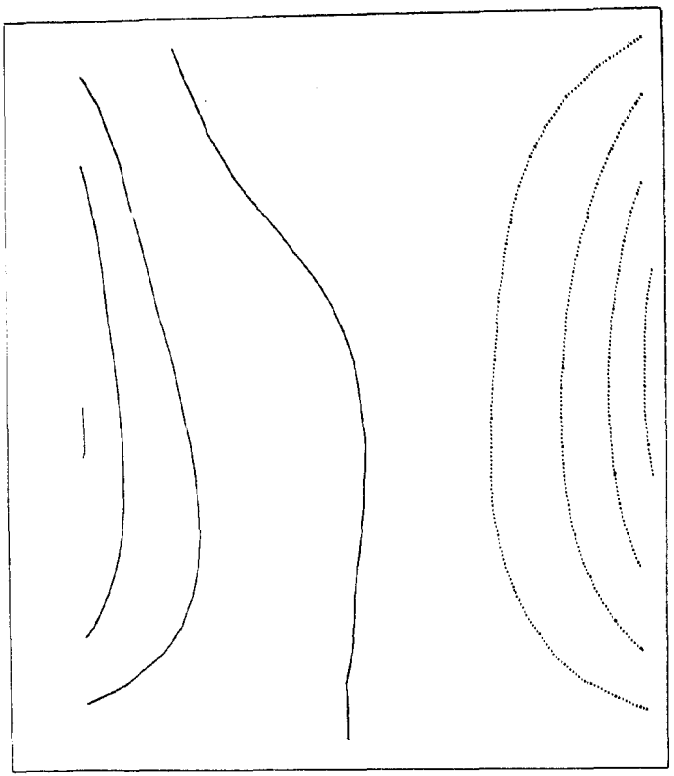

FIG. 5. Contour lines of the north-south component of depth-weighted velocity, N_2, (excluding the first two western zones) at day 1. Solid lines indicate zero or positive values while broken lines indicate negative values. (This plotting convention holds for all contour plots.) The contour interval is 0.015 km²/h.

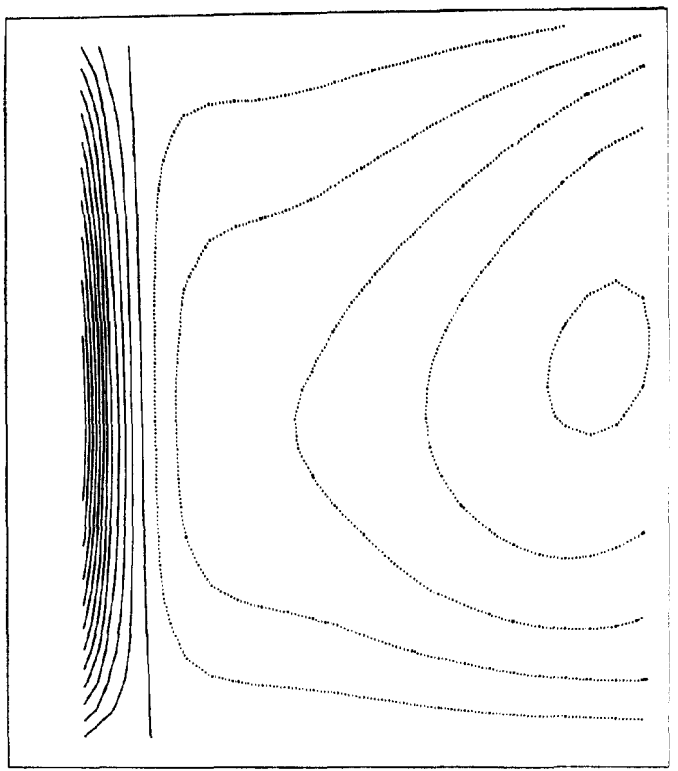

FIG. 6. Contour lines of N_2 at day 5.

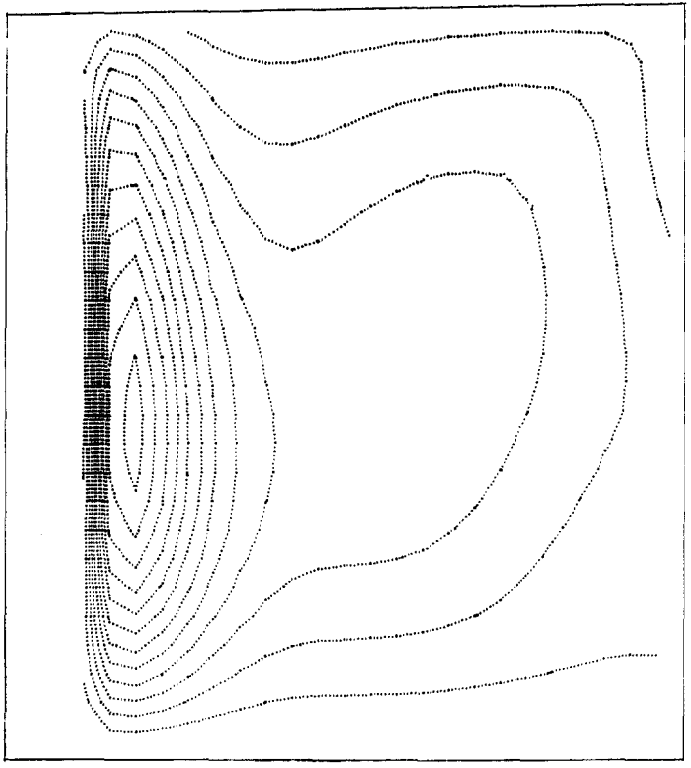

FIG. 7. Contour lines of N_2 at day 9.

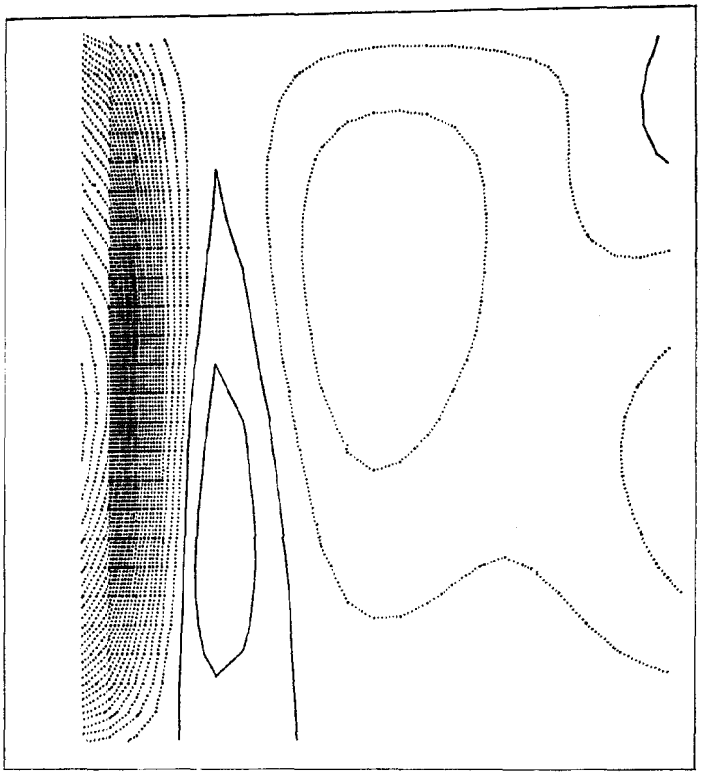

FIG. 8. Contour lines of N_2 at day 13.

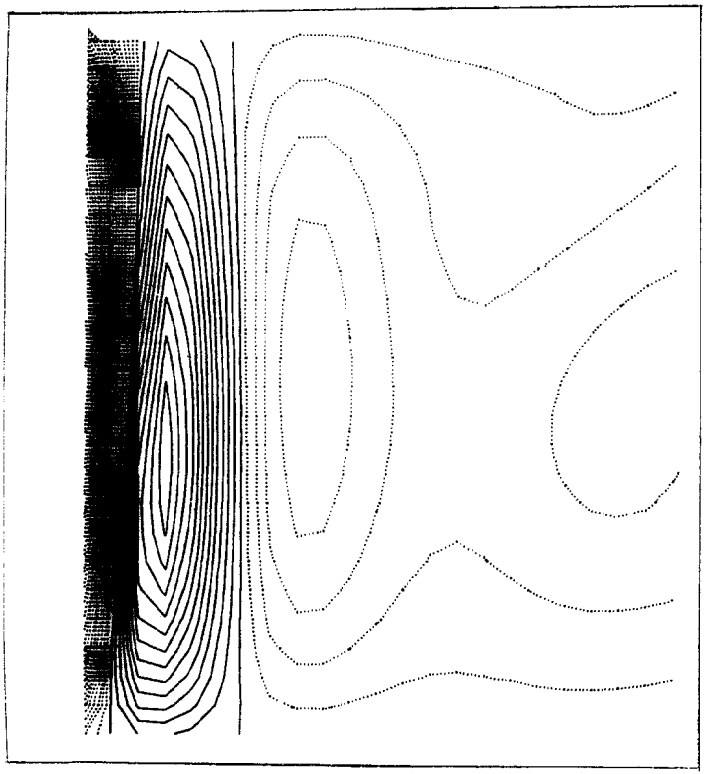

FIG. 9. Contour lines of N_2 at day 17.

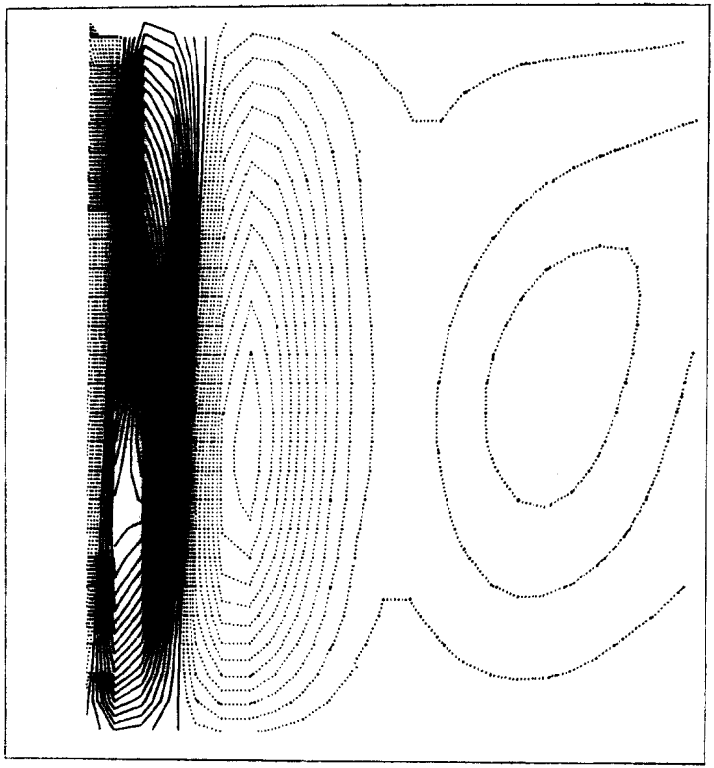

FIG. 10. Contour lines of N_2 at day 21.

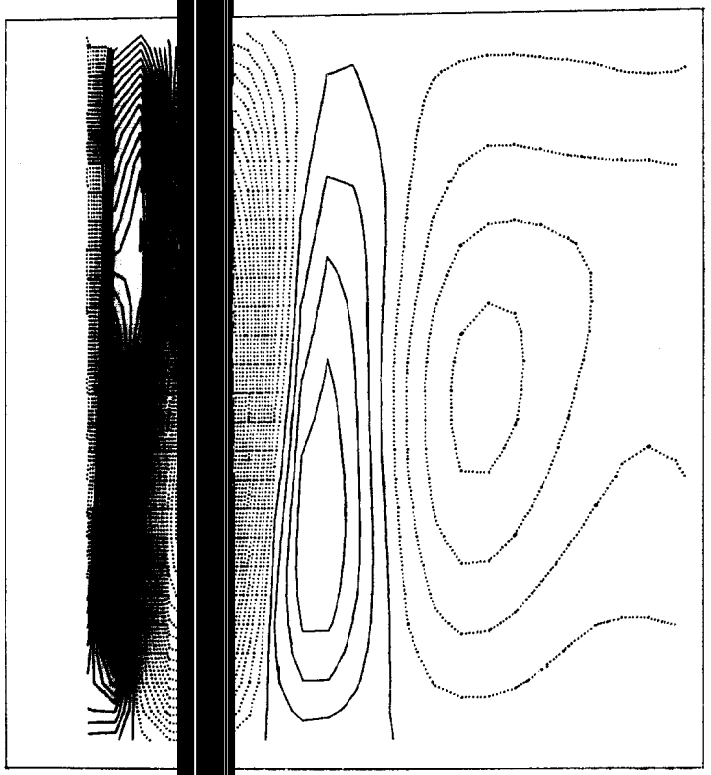

F . Contour lines of N_2 at day 25.

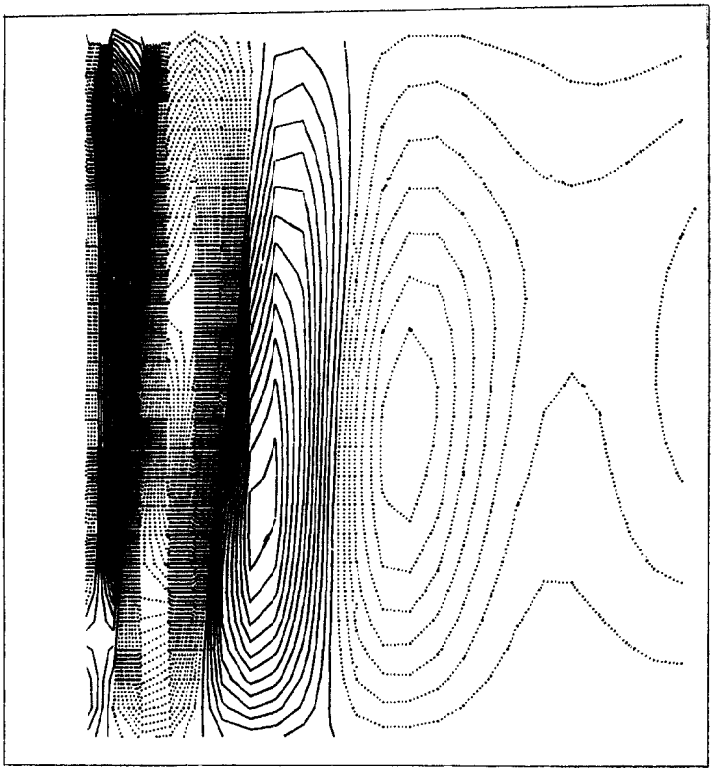

FIG. 12. Contour lines of N_2 at day 29.

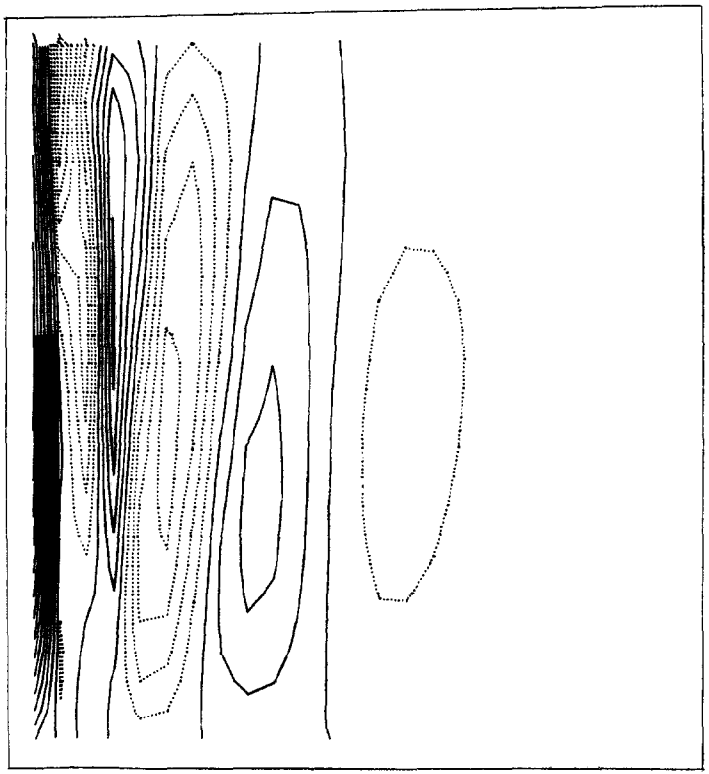

FIG. 13. Contour lines of N at day 29. The contour interval is 0.08 km²/h.

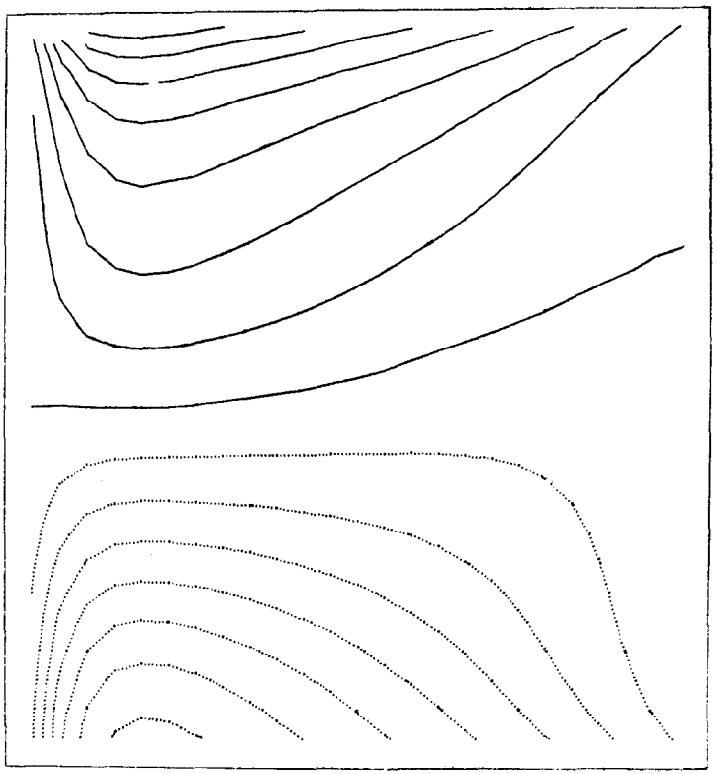

FIG. 14. Contour lines of the east-west component of depth-weighted velocity, M, at day 5. The contour interval is 0.025 km²/h.

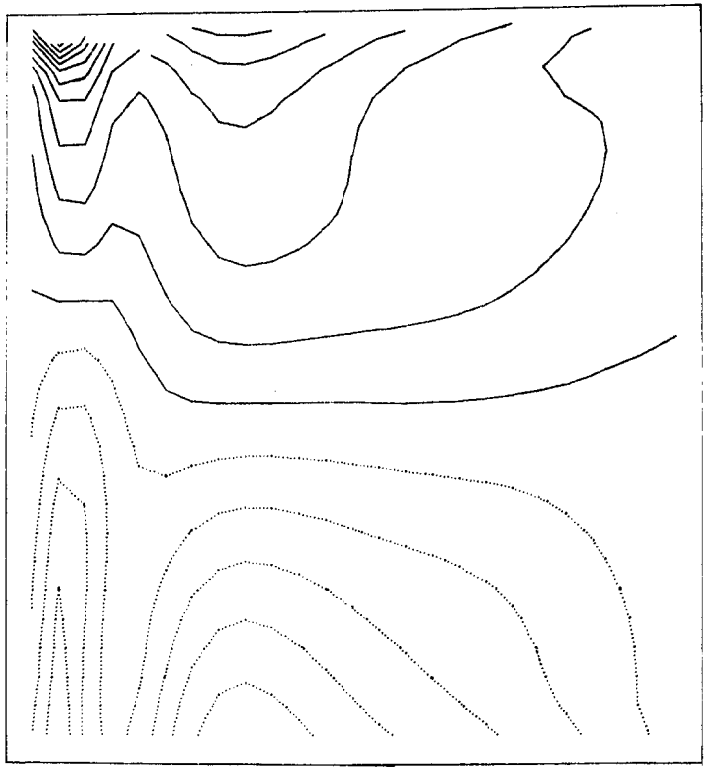

FIG. 15. Contour lines of M at day 17.

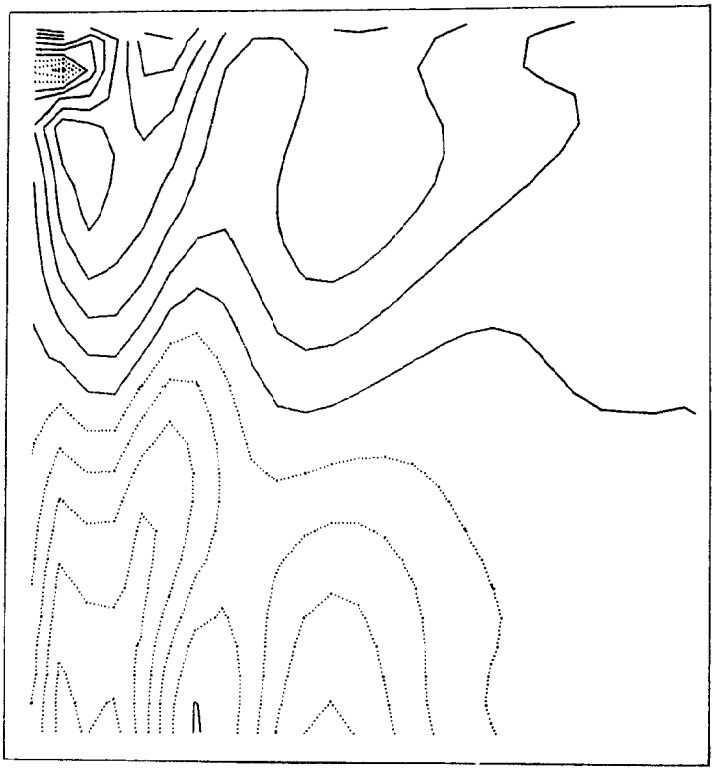

FIG. 16. Contour lines of M at day 29.

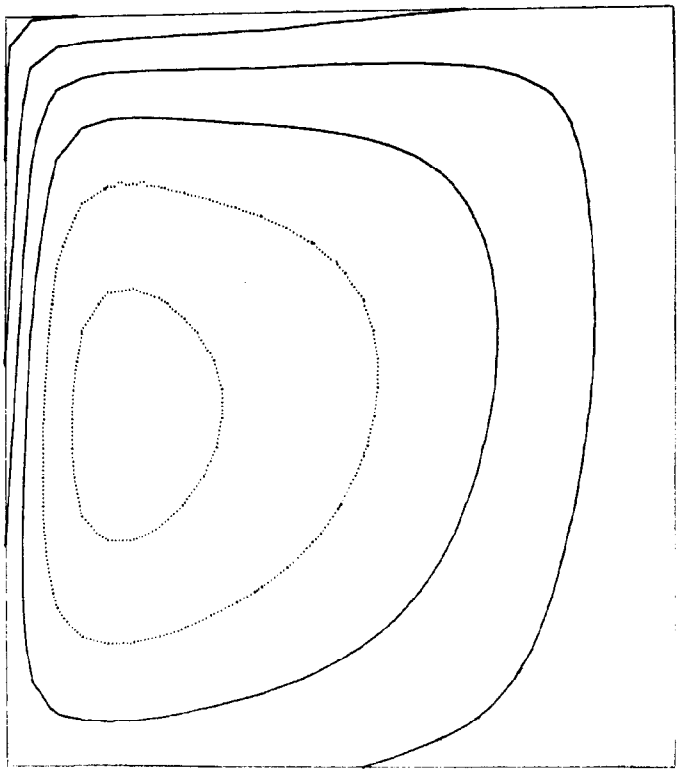

FIG. 17. Contour lines of the surface height anomaly, h, at day 5. Broken lines correspond to negative values of h which correspond to wave crests. The contour interval is 30 cm.

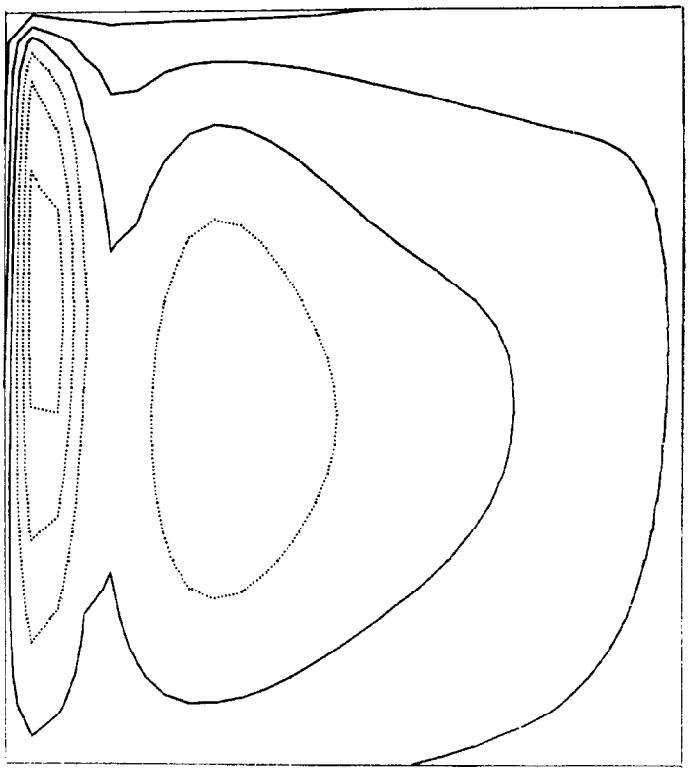

FIG. 18. Contour lines of h at day 17.

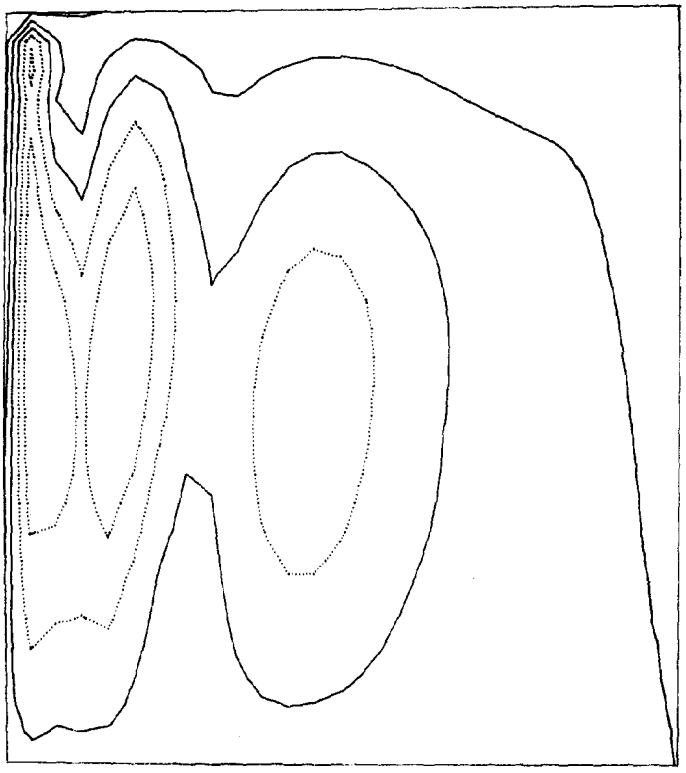

FIG. 19. Contour lines of h at day 29.

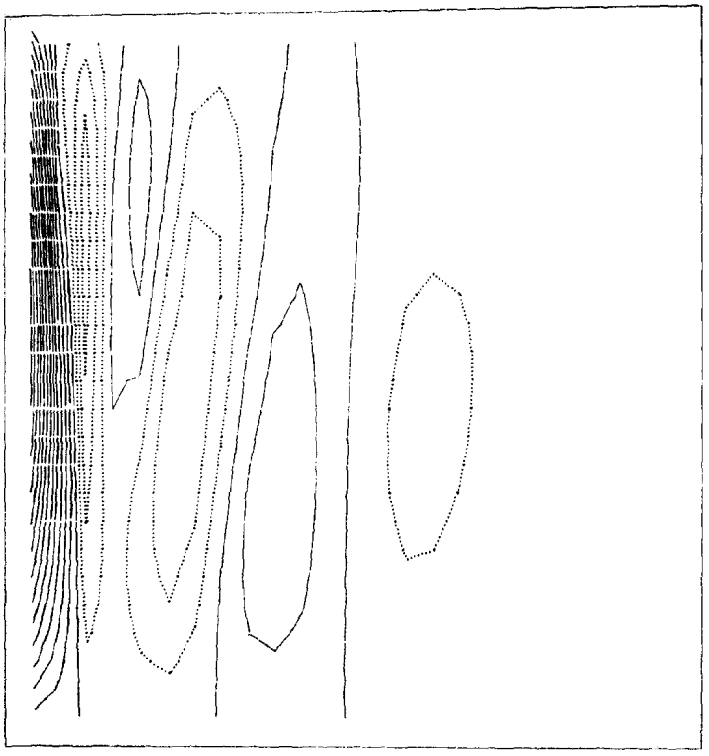

FIG. 20. Contour lines of N at day 29 (linear viscosity). The contour interval is 0.08 km²/h.

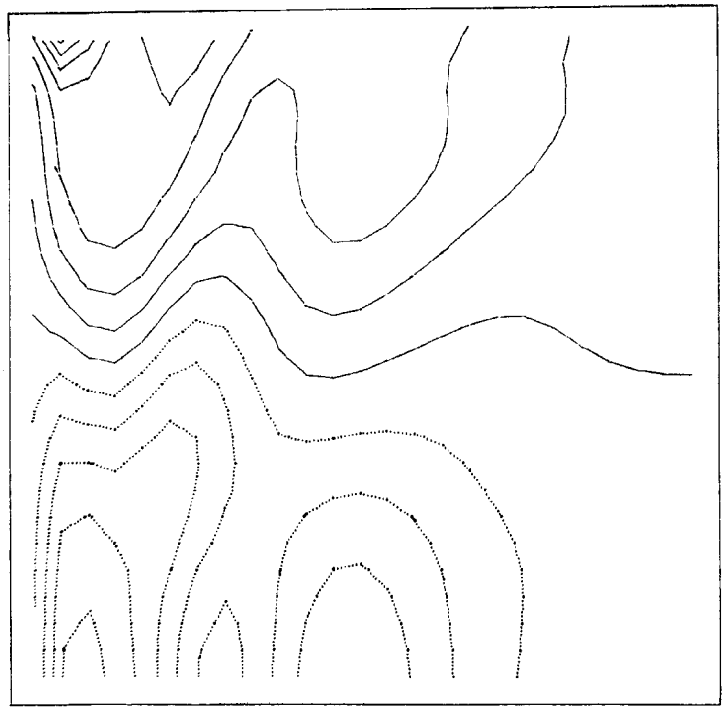

FIG. 21. Contour lines of M at day 29 (linear viscosity).

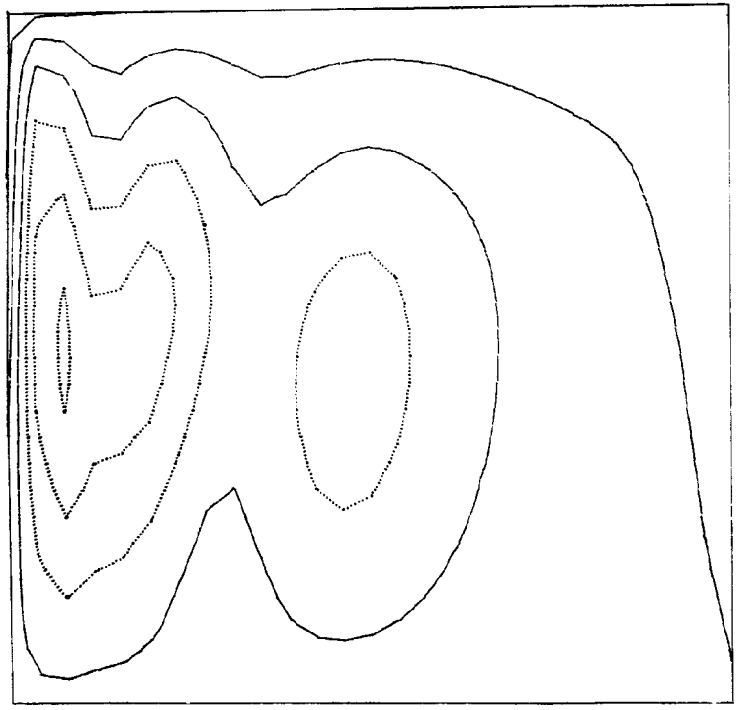

FIG. 22. Contour lines of h at day 29 (linear viscosity).

The most striking difference between the two solutions is found in a comparison of the M fields at day 29 (Figs. 16 and 21). Over most of the basin the solutions are qualitatively the same, but the gradients of M are greater for the nonlinear case than the linear. In addition, a small anticyclonic gyre appears in the north-west corner of the nonlinear solution—it never appears in the linear solution. This gyre materializes at day 25, intensifies to day 32 then slowly decays until it disappears at day 69.

A comparison of the surface height fields (Figs. 19 and 22) at day 29 emphasizes the above mentioned differences between the two cases.

The anticyclonic gyre appears in Bryan's rigid-lid, time-averaged solutions [1] when the Reynolds number becomes large enough. This indicates that it is not the nonlinear eddy viscosity itself that causes the gyre to develop here; rather the nonlinear formulation permits a lower (on the average) eddy viscosity coefficient and this introduces less small-scale viscous damping into the solution (see Appendix I). Since the value of the linear eddy viscosity coefficient necessary for computational stability is proportional to some power of the mesh increment [14], a refinement of the mesh (and corresponding decrease in the eddy viscosity coefficient) should allow the gyre to develop in the linear (viscosity) case.

Summary

We have considered a homogeneous wind-driven flow in a basin on a beta-plane as an initial value problem. A numerical algorithm using forward time differences and Marchuk's time-splitting technique has been proposed for solving this problem. A linear stability analysis of the system of finite difference equations has been carried out; it results in an estimate for the permissible time step that is large by a factor of three.

Two numerical solutions have been found for integration times to 29 days. The first solution is obtained with a standard linear eddy viscosity and it is quite similar to the solution found by Gates. The second solution is obtained with a nonlinear eddy viscosity based on a dimensional argument from two-dimensional turbulence theory. This second solution differs from the first in that the interior flows are more intense and in that the western boundary current is modified by the addition of a transient anticyclonic gyre in the north-west corner of the basin.

APPENDIX. A Nonlinear Eddy Viscosity

The need for nonlinear dissipative mechanisms in numerical hydrodynamic calculations has previously been cited by Smagorinsky [15] and Leith [14] who based their arguments on three and two dimensional theories of turbulence. In a

two-dimensional calculation such as that presented here the vorticity enters the system in large scales and cascades (via the nonlinear advection term) outward to smaller scales. It eventually reaches scales comparable to the mesh size and in this region contributes to a numerical aliassing error that cannot be removed by decreasing Δt [16]. The only way to eliminate this error is to remove vorticity from small scales—in a configuration-space calculation such as that reported on here, this is usually accomplished by including viscous terms (an eddy viscosity) in the equations of motion. Unfortunately, linear eddy viscosities are not very selective, and they damp large scales as well as small scales. This may be seen by referring to Fig. 23 in which the amplitude damping due to truncation errors and to viscous

$$\frac{\partial u}{\partial t} + u\frac{\partial u}{\partial x} = \kappa \frac{\partial^2 u}{\partial x^2}.$$

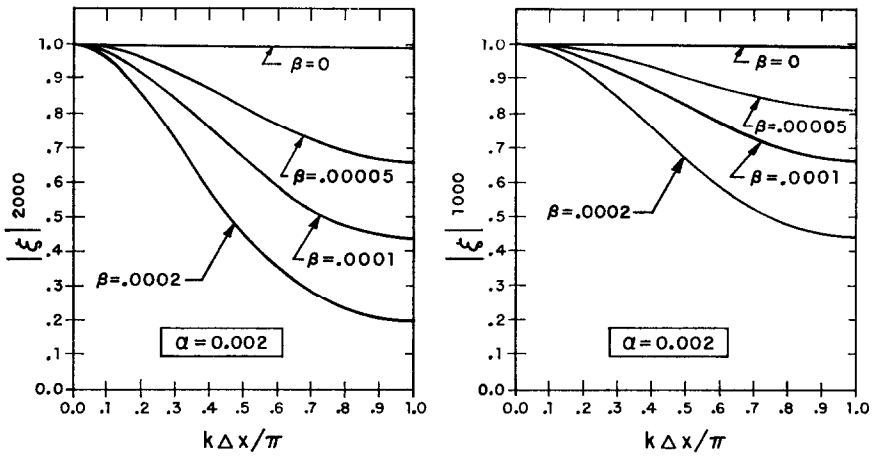

FIG. 23. The eigenvalue of the finite difference operator Λ after 2000 and 1000 time steps (see appendix). The parameters are: $\alpha = u\Delta t/\Delta x$ and $\beta = \kappa\Delta t/\Delta x^2$.

Applying the difference equations used here to this equation, one arrives at the recursion relation

$$u_j^{n+1} = \Lambda u_j^n,$$

where Λ is a finite difference operator. Assuming u to be an eigenvector of Λ,

$$u(j\,\Delta x, n\,\Delta t) = \epsilon^{ikj\Delta x}$$

results in

$$u_j^{n+1} = \xi(k) u_j^n,$$

where

$$\xi(k) = 1 - (\alpha^2 + 2\beta)(1 - \cos k\Delta x) - i\alpha \sin k\Delta x$$

is the eigenvalue of A and where we have used the notation of Section V.

Numbers characterising the calculations presented here are: $\alpha = 0.002$ and $\beta = 0.0001$. Using these values (also $\beta/2$, 2β, and $\beta = 0$) we have constructed Fig. 23 and show there the magnitude of $\xi(k)$ vs $k\Delta x/\pi$ after 1000 and 2000 calculation cycles. It is seen that the linear viscosity does not completely remove the smallest scales of motion and that it also strongly damps the larger scales. (Somewhat arbitrarily, the distinction between small and large is taken to be $k\Delta x = \pi/2$.)

We have thus indicated that: some mechanism is needed to remove vorticity from small scales; that linear eddy viscosities are the usual choice; and, that they are inadequate. This inadequacy is apparently alleviated to a great extent by the use of nonlinear eddy viscosities in which the magnitude of the viscous coefficient depends on local flow conditions. Although it is clearly impossible to demonstrate this by a linear analysis, it is possible to observe the effects of these nonlinear eddy viscosities on solutions and to infer conclusions from these observations. For example, it is obvious in the solutions presented here that the nonlinear dissipation has introduced less damping into large scales and has permitted small scales to evolve while at the same time it has prevented computational instability from developing.

The eddy viscosity used here is one postulated by Leith [14]; it was used in a previous ocean circulation calculation [6]. Dimensional arguments based on the cascade of vorticity in two dimensions lead to the form

$$\kappa = \tilde{\alpha}^{3/2} L^3 \mid \nabla\omega \mid,$$

where $\tilde{\alpha}$ is a dimensionless coefficient, L is the mesh spacing and ω is the relative vorticity. It has been found that computational stability is a sharp function of $\tilde{\alpha}$. The solution presented here was obtained for $\tilde{\alpha} = 0.05$, however, for $\tilde{\alpha} = 0.075$ the same problem went unstable after about 1500 cycles.

ACKNOWLEDGMENT

I thank Dr. H. Ellsaesser for several enlightening discussions held during the course of this investigation.

This work was performed under the auspices of the United States Atomic Energy Commission.

REFERENCES

1. K. BRYAN, A numerical investigation of a nonlinear model of a wind-driven ocean, *J. Atmospheric Sci.* **20** (1963), 594–606.
2. W. L. GATES, A numerical study of transient Rossby waves in a wind-driven homogeneous ocean, *J. Atmospheric Sci.* **25** (1968), 3–22.
3. A. R. ROBINSON, ED., "Wind-Driven Ocean Circulation," Blaisdell, New York, 1963.
4. R. COURANT, K. O. FREIDRICHS, H. LEWY, Über die Partiellen Differenzengleichungen der Mathematischen Physik, *Math. Ann.* **100** (1928). See also NYO-7689, a translation by Phyllis Fox (1956).
5. P. D. THOMPSON, "Numerical Weather Analysis and Prediction," Macmillan, New York, 1961.
6. W. P. CROWLEY, A global numerical ocean model: Part I, *J. Comp. Phys.* **3** (1968), 111–138.
7. G. FISCHER, On a finite difference scheme for solving the nonlinear primitive equations for a barotropic fluid with application to the boundary current problem, *Tellus* **17** (1965), 405–412.
8. W. H. MUNK, On the wind-driven ocean circulation, *J. Meteor.* **7** (1950), 79–93.
9. W. P. CROWLEY, Numerical Advection Experiments, *Monthly Weather Rev.* **96** (1968), 1–11.
10. G. I. MARCHUK, Theoretical model for weather forecasting, *Akad. Nauk. SSSR Dokl.* **155** (1964) 1062–1065.
11. H. STOMMEL, The westward intensification of wind-driven ocean currents, *Trans. Amer. Geophys. U.* **29** (1948), 200–206.
12. M. S. LONGUET-HIGGINS, Planetary waves on a rotating sphere. II, *Proc. Roy. Soc.* **248A** (1965) 40–68.
13. G. VERONIS, Wind-driven circulation—Part 2. Numerical solutions of the nonlinear problem, *Deep Sea Res.* **13** (1966), 31–55.
14. C. E. LEITH, "Numerical Simulation of Turbulent Flow," in "Properties of Matter Under Unusual Conditions," (H. Mark and S. Fernbach, Eds.), Interscience Publishers Inc. New York, 1969.
15. J. SMAGORINSKY, "General circulation experiments with the primitive equations. I. The basic experiment, *Mon. Weather Rev.* **91** (1963), 99–164.
16. N. A. PHILLIPS, "An Example of Non-Linear Computational Instability," in "The Atmosphere and Sea in Motion," Rockefeller Inst. Press, New York, 1959.